ACES Asian Chemical Editorial Society

doi.org/10.1002/asia.70385

CHEMISTRY AN ASIAN JOURNAL Research Article

www.chemasianj.org

Fluorine-Modulated Hierarchical NiFeCo-LDHs for Efficient and Stable Bifunctional Water Splitting in Alkaline and Seawater Media

Zhipeng Su,[a] Boyao Zhang,[a] Yibo Wang,[a] Xin Li,[a] Huiya Zhou,[a] Yongqi Tian,[a] Jun Xiang,[a] Rong-Da Zhao,*[a] and Lihua Miao*[b]

This work synthesized a hierarchical-structured nickel-iron-cobalt layered double hydroxide (NiFeCo-LDHs) with heterointerfaces via a controllable hydrothermal method. The ternary metal system optimized the charge transport pathways through atomic-level synergy specifically the multivalent synergy. Furthermore, the high electronegativity of fluorine modulated the electronic conduction kinetics of NiFeCo-LDHs. Electrochemical testing demonstrated that, Owing to Ni^{2+} doping and fluorine atom modulation of LDH interlayer spacing, the NiFeCo-LDHs exhibited significantly enhanced hydrogen evolution reaction (HER) performance in 1.0 M KOH electrolyte. The HER overpotential is 74.3 mV at a current density of −10 mA cm^{-2}. As a bifunctional electrode, it required an OER overpotential of only 204.3 mV to achieve 10 mA cm^{-2}, and its stability remains robust even after 12 h of cycling. Notably, the catalyst maintains impressive performance for both HER and OER in seawater environments.

1. Introduction

The increasingly acute depletion of fossil fuels, escalating energy crises, and intensifying environmental problems profoundly threaten human survival. Achieving coordinated development among society, the economy, and the environment has become a globally urgent challenge.[1–6] Current mainstream clean energy technologies, such as lithium-ion batteries and photovoltaics, primarily address the challenges of energy storage and electricity generation. However, they are incapable of directly producing high-energy-density, zero-carbon chemical fuels. In contrast, hydrogen stands out as an ultimate clean energy carrier, and its large-scale production is critically dependent on efficient hydrogen generation via water electrolysis. Therefore, we posit that the advancement of water electrolysis technology represents a core pathway to resolving the prevailing "energy-environment" dilemma. Consequently, developing stable and efficient electrocatalysts for water electrolysis—a key technology for converting renewable electricity into storable hydrogen fuel is imperative. In particular, bifunctional catalysts capable of concurrently driving both the hydrogen evolution reaction (HER) and oxygen evolution reaction (OER) are highly desired to simplify system architecture and reduce costs compared to using separate monofunctional catalysts. Substantial research efforts have been devoted this area,[7] leveraging the abundance of water resources within renewable energy systems and the potential for high-purity hydrogen production. Among these efforts, water electrolysis technology stood out, comprising two half-reactions: the hydrogen evolution reaction (HER) and the oxygen evolution reaction (OER).[8–10] Historically, precious metal-based electrocatalysts such as Pt and RuO_2/IrO_2 have been extensively investigated due to their exceptional water-splitting performance.[11,12] However, their scarcity, high cost, and limited durability hindered their practical large-scale applications.[13,14] Therefore, developing highly active, cost-effective non-precious metal catalysts represented a critical pathway toward achieving efficient energy conversion.[15–19]

Among the diverse electrocatalysts, transition metal hydroxides represent promising catalysts for overall water splitting. Within this category, layered double hydroxides (LDHs) have been extensively investigated due to their layered structure, high specific surface area, excellent interfacial interfacial properties, and tunable chemical composition.[20–25] The hydrothermal method stands as one of the simplest and most effective techniques for synthesizing electrode materials. Extensive studies confirm that under hydrothermal conditions, mixed M^{2+} and M^{3+} salt solutions with slow-releasing hydrolyzing agents (e.g., urea) facilitate the two-dimensional crystallization of layered double hydroxides.

Recently, Lemoine et al. demonstrated that fluorination yielded amorphous $NiFe_2F_{4.4}O_{1.8}$ oxyfluoride with outstanding activity and stability in alkaline electrolyte (showing only 40 mV activity loss after 50–250 h of continuous operation).[26] Strategies like metal doping influence nucleation rates and alter material morphology. For instance, Lu et al. hydrothermally synthesized a three-dimensional Ni-Fe-Co ternary LDH nanosheet array electrocatalyst. Introducing iron into the nickel-cobalt

[a] Z. Su, B. Zhang, Y. Wang, X. Li, H. Zhou, Y. Tian, J. Xiang, R.-D. Zhao
School of Materials Science and Engineering, Liaoning University of Technology, Jinzhou 121001, P.R. China
E-mail: rongdazhaoln@126.com

[b] L. Miao
School of Medical Information Engineering, Shenyang Medical College, Shenyang, Liaoning 110043, P.R. China
E-mail: lihuamiao@163.com

Supporting information for this article is available on the WWW under https://doi.org/10.1002/asia.70385

hydroxide matrix formed ternary LDHs exhibiting nanoarray architecture. Theoretical analysis confirmed that adjusting the Ni/Co/Fe ratio induced significant microstructural changes in the catalyst. Attributable to its unique nanostructure, the catalyst exhibited superior oxygen evolution reaction (OER) performance, achieving an overpotential of 222 mV at 20 mA cm^{-2} in 1.0 M KOH, with a Tafel slope of 61.22 mV dec^{-1} and a maximum specific capacitance of 239 Fg^{-1}.[27]Zhang et al. fabricated a poly-metallic hybrid film (NiFeCo/SSM) via co-sputtering, which was subsequently transformed into $NiFeCoSe_2$ nanosheets through an alloying-dealloying-selenization process. Here, Co and Fe atoms partially substituted Ni atoms within the NiS_2 lattice. The resultant NiFeCo/SSM delivered efficient OER performance in 1.0 M KOH electrolyte, requiring overpotentials of 228 mV at 20 mA cm^{-2} and 268 mV at 50 mA cm^{-2}, alongside a low Tafel slope of 69.8 mV dec^{-1}. Moreover, the electrode demonstrated substantial catalytic stability over 24 h, with its initial nanosheet morphology well preserved post-durability testing.[28]

Building upon the efforts to overcome the bottlenecks of poor conductivity, limited active sites, and insufficient cycling stability in metal hydroxides (including bimetallic systems), this study employs a simple and low-cost one-step hydrothermal method to grow NiFeCo-LDHs on nickel foam under a high-concentration fluorine atmosphere, where Ni plays a synergistic role in the NiFeCo-LDHs structure through doping. The prepared NiFeCo-LDHs-1 demonstrates bifunctional performance superior that of most reported electrocatalysts in 1.0 M KOH electrolyte. It exhibited a low HER overpotential of 74 mV at −10 mA cm^{-2}, with a Tafel slope of 149.82 mV·dec^{-1} and an OER overpotential of 217.3 mV at 20 mA cm^{-2} with a Tafel slope of 86.53 mV·dec^{-1}, indicating rapid reaction kinetics. In alkaline seawater electrolytes, the overpotentials reach 109.5 and 207.5 mV at current densities of −10 and 20 mA cm^{-2} for HER and OER, respectively. Furthermore, the material sustains a low cell voltage of 1.956 V at 100 mA cm^{-2} with outstanding cycling stability, maintaining this voltage at 1.964 V at 100 mA cm^{-2} over 30-h continuous operation.

2. Results and Discussion

Initial analysis focused on the crystal structure of the synthesized products. First, the crystal structure information of the synthesized products was analyzed. The X-ray Diffraction (XRD) pattern is presented in Figure 1a. The strong diffraction peaks observed at 2θ values of 44.4°, 51.6°, and 76.1° are characteristic of the nickel foam substrate. The diffraction peaks located at 2θ = 11.6°, 23.4°, 33.2°, 34.1°, 35.1°, 36.6°, 46.2°, 60.5°, and 63.4° can be well-indexed to the (003), (006), (101), (012), (009), (104), (018), (113), and (1013) crystal planes of the CoFe-LDH phase (JCPDS no. 50–0235).Meanwhile, the peaks at 18.8° and 71.5° correspond to the diffraction of $Co(OH)_2$ (JCPDS no. 45–0031). It is observable that when the molar ratio in NiFeCo-LDH is not equimolar, the intensity of these peaks increases significantly. This indicates a greater formation of $Co(OH)_2$, which can cover the catalyst surface and lead to a decline in performance. The shift in the NiFeCo-LDH peaks relative to the standard CoFe-LDH pattern is attributed to changes in the interlayer spacing caused by Ni doping. Upon comparing the XRD spectra of NiFeCo-LDHs with different Ni:Fe:Co molar ratios, it was found that the characteristic peaks of the CoFe-LDH phase were enhanced as the molar proportion of Co or Fe increased. This result suggests that while NiFeCo-LDHs were successfully prepared on nickel foam via a one-step hydrothermal method, a deviation from an optimal molar ratio weakens the role of Ni doping within the CoFe-LDH structure. This weakening effect hinders the formation of a well-defined NiFeCo-LDH crystal structure, reduces the number of active sites and the active surface area, and consequently degrades the material's performance.

To elucidate electronic structure evolution, XPS measurements probed the surface chemical states of the catalysts. The Ni 2p spectrum (Figure 1b) was deconvoluted into two nickel species: Ni^{2+} and Ni^{3+}. The binding energies of 857.34 and 856.17 eV corresponded to Ni^{3+} and Ni^{2+} in the Ni $2p_{3/2}$ orbital, respectively, while the binding energies of 875.88 and 874.05 eV correspond to Ni^{3+} and Ni^{2+} in the Ni $2p_{1/2}$ orbital. Peaks at 880.61 and 862.57 eV can be assigned to satellite features (abbreviated as Sat.), revealing that the majority of Ni exists in the form of Ni^{2+} and Ni^{3+} ions. The Fe 2p spectrum (Figure 1c) exhibits Fe^{3+} (711.32 eV) and Fe^{2+} (713.64 eV) in the Fe $2p_{3/2}$ region, with satellites at 717.79 and 720.74 eV. The Fe $2p_{1/2}$ region shows Fe^{3+} at 724.62 eV and Fe^{2+} at 726.84 eV, alongside satellite features at 728.78 and 734.43 eV. The Co 2p spectrum of the sample (Figure 1d) displays characteristic peaks for both Co $2p_{3/2}$ and Co $2p_{1/2}$, along with two satellite peaks. In the region corresponding to the Co $2p_{3/2}$ peak, the maximum at 781.84 eV is assigned to Co^{3+}, while the peak at 785.63 eV is ascribed to Co^{2+}, with the satellite peak appearing at 788.92 eV. For the Co $2p_{1/2}$ peak, the component centered at 797.56 eV corresponds to Co^{3+}, that at 802.50 eV to Co^{2+}, and the satellite peak occurs at 804.23 eV. These observations demonstrate the coexistence of both Co^{3+} and Co^{2+} species in the sample.[29,30] The F 1 s spectrum (Figure 1e) displays a singular peak at 684.72 eV, verifying F^- incorporation. Deconvolution of the O 1 s spectrum (Figure 1f) resolves three components: The peak observed at 532.9 eV is typically associated with low-coordination oxygen species (e.g., surface hydroxyl groups or terminal oxygen) related to surface defect sites or edges.[31] The peak located at 531.94 eV corresponds to chemisorbed and physisorbed water molecules at the surface and within the near-surface region.[32] The peak positioned at 529.92 eV is assigned to oxygen vacancies or lattice oxygen defects within the structure.[33]

Figure 2a,b presents the morphological characteristics of the NiFeCo-LDHs-1 material via scanning electron microscopy (SEM) imaging. The low-magnification image (Figure 2a) reveals a uniform three-dimensional lamellar architecture, where adjacent nanosheets stack to form an open-channel scaffold, a structure conducive to charge transport.[34–36] The high-magnification image (Figure 2b) further demonstrates that the nanosheets are densely packed and interlocked in a disordered manner. The rough edges that developed during growth significantly increase the active surface area, which facilitates ion adsorption during the electrochemical process. Figure S3a–b display the SEM

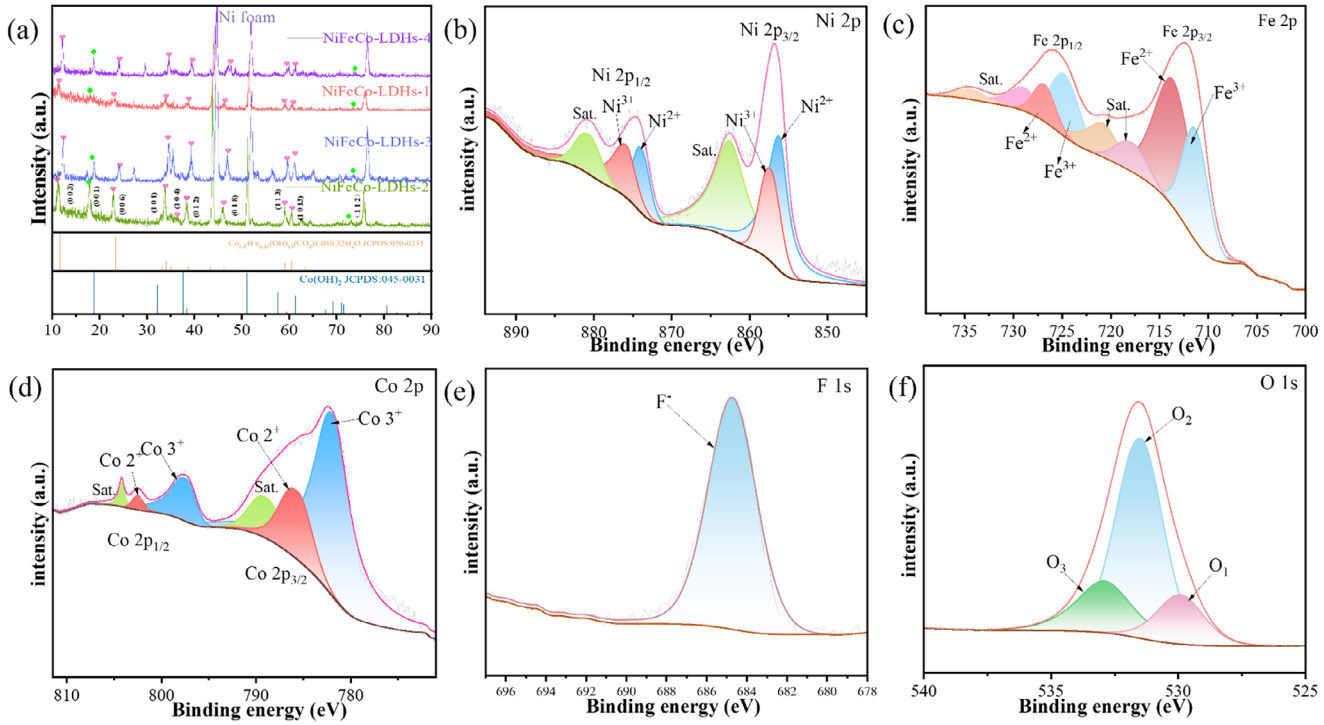

Figure 1. Structure characterization of as-prepared electrode materials. a) XRD patterns. b) XPS of Ni 2p, c) Fe 2p, d) Co 3d, e) F 1 s and f) O 1 s.

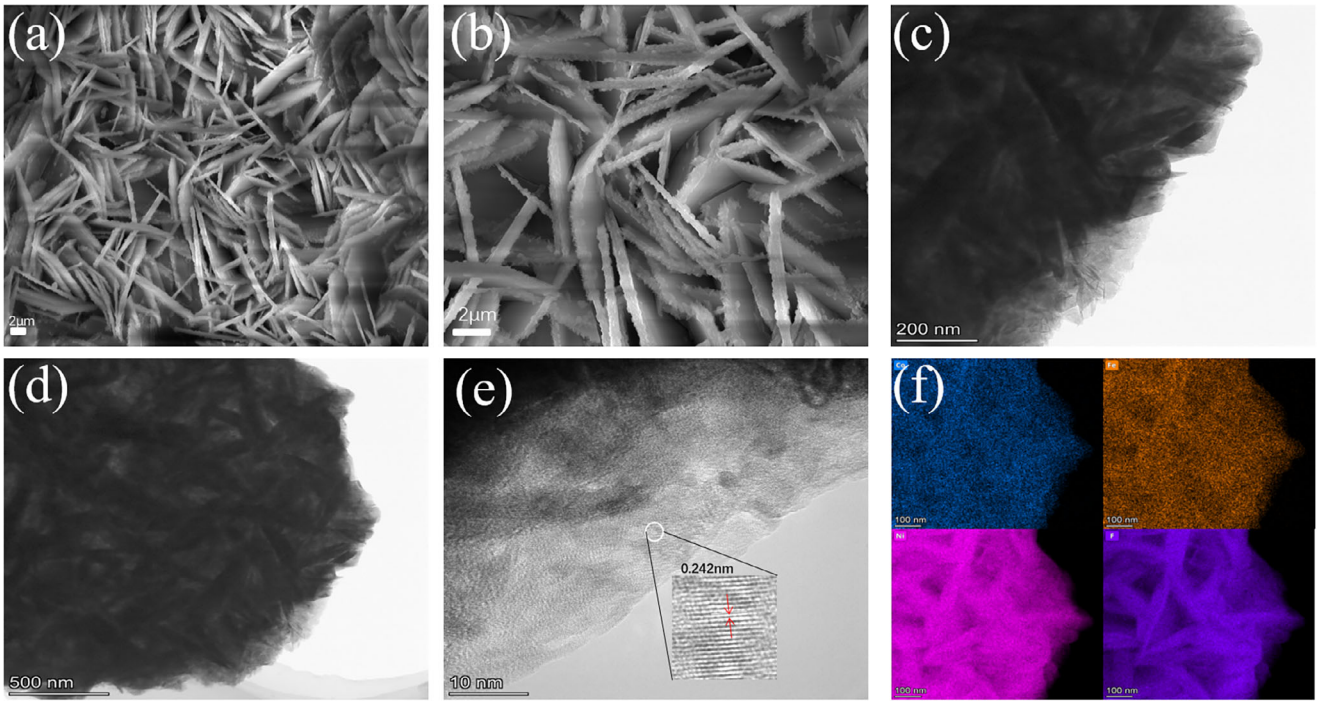

Figure 2. Structure characterization of the NiFeCo-LDHs-1 catalysts. a), b) SEM images. c–e) TEM images, f) elemental mapping images.

images of NiFeCo-LDH-2. At low magnification, the nanosheets are densely distributed, while at high magnification, the sheet-like structures appear thicker with a smoother surface, indicating a smaller active area. Figure S3c–d show the nanosheet structure of NiFeCo-LDH-3. It is evident that as the iron concentration increases or when the Fe:Co ratio is equal, the degree of rough particles on the nanosheet edges also increases, although this leads to an increase in nanosheet thickness. Figure S3e–f show the nanosheet structure of NiFeCo-LDH-4, which has the thinnest nanosheets and a smooth surface due to the highest Co content

and lower Fe content. The variation in Fe content changes the crystal growth kinetics, which determines the roughness of the nanosheet edges and, consequently, influences the catalytic efficiency. This hierarchical sheet-like structure provides an effective pathway for electrolyte permeation and charge transport, thereby enhancing the material's electrochemical performance. The cross-linked nanosheet network forms a continuous 3D scaffold, which helps improve the material's structural stability. The microstructural features of the NiFeCo-LDHs-1 sample were further analyzed using transmission electron microscopy (TEM) and high-resolution TEM (HRTEM). The TEM image (Figure 2c) further confirms the nanosheet structure with a distinct rough surface, which contributes to an increased specific surface area. The HRTEM image (Figure 2d) shows a thin film covering the nanosheet surface. The corresponding HRTEM image in Figure 2e reveals lattice fringes with an interplanar spacing of 0.242 nm, corresponding to the (1 0 4) crystallographic plane of the CoFe phase.Ni doping induces electron redistribution, increasing the local charge density. This effect optimizes the adsorption capacity for hydrogen and oxygen intermediates, thereby enhancing electrocatalytic activity. Furthermore, the energy-dispersive X-ray spectroscopy (EDS) elemental mapping of the NiFeCo-LDH-1 product (Figure 2f) confirms the homogeneous distribution of Ni, Fe, Co, O, and F elements throughout the nanosheet.

The hydrogen evolution reaction (HER) performance of the synthesized electrocatalysts was systematically evaluated using a three-electrode setup in 1.0 M KOH electrolyte. Ohmic drop (*IR*) compensated LSV curves acquired at 2 mV s^{-1} (Figure 3a) demonstrate that NiFeCo-LDHs-1 achieves an ultralow overpotential of 74 mV at -10 mA cm^{-2}, significantly lower than NiFeCo-LDHs-2 (105.7 mV), NiFeCo-LDHs-3 (130.7 mV), and NiFeCo-LDHs-4 (91.7 mV). This superior activity at the Ni:Fe:Co molar ratio of 1:1:1 highlights the enhanced HER reactivity induced by fluorine regulation and nickel doping. Further kinetic analysis reveals a Tafel slope of 149.82 mV dec^{-1} for NiFeCo-LDHs-1 (Figure 3b), markedly lower than other variants, confirming accelerated reaction kinetics. Electrochemical active surface area (ECSA), quantified via double-layer capacitance (Cdl), shows NiFeCo-LDHs-1 possesses the highest Cdl of 6.53 mF cm^{-2} (Figure 3c), corresponding to abundant exposed active sites that bolster catalytic performance.[18,34] Electrochemical impedance spectroscopy (EIS) analysis (Figure S1a) reveals a minimized semicircle diameter in the high-frequency region for NiFeCo-LDHs-1, indicative of reduced charge transfer resistance (Rct) due to Ni doping. Bode phase plots (Figure S1b) collected from −10 to −100 mA cm^{-2} exhibit progressively decreasing phase angles at low frequencies, signaling reduced Rct at higher current densities that promotes charge transfer efficiency.[37] Figure 3d utilizes Electrochemical Impedance Spectroscopy (EIS) to investigate the kinetic behavior of the catalysts during the Hydrogen Evolution Reaction (HER). By fitting the Nyquist plots with an equivalent circuit model, the charge transfer resistance (Rct) and solution resistance (Rs) can be obtained. The inset in Figure 3d shows the equivalent circuit diagram used for the fitting. A smaller Rct value indicates faster interfacial charge transfer, more favorable reaction kinetics, and consequently, higher catalytic activity. The Rct value for NiFeCo-LDHs-1 was 7.976 Ω. The reason this value is higher than that of other catalysts may be that in the low-potential region at high frequencies, reactant ions (such as H^+, OH^-) in the electrolyte are rapidly consumed at the electrode surface, leading to a sharp drop in the local surface concentration. The resulting concentration gradient enhances the driving force for Fickian diffusion; however, because a stable laminar flow layer has not yet formed in the diffusion path, the actual ion diffusion rate is insufficient, manifesting as a rapid increase in diffusion impedance.

To elucidate the underlying microkinetics, distribution of relaxation times (DRT) analysis was performed on NiFeCo-LDHs-1 (Figure 3e). This technique employs mathematical deconvolution of EIS data through Tikhonov regularization, resolving impedance contributions into distinct relaxation processes characterized by time constants (τ), thereby identifying the dominant rate-determining steps during HER operation. Each identified relaxation peak in the distribution corresponds to distinct electrochemical processes within the electrode-material system, including interfacial charge transfer, ion migration, and electric double-layer (EDL) charging, which proceed at different characteristic rates.[38] The relaxation time τ is mathematically defined as the product of interfacial resistance (R) and capacitance (C), expressed by Equation 1:

$$\tau = RC \quad (1)$$

The relaxation time τ characterizes the transition duration from transient to steady state in electrochemical systems, where a larger τ correlates with lower-frequency responses and slower kinetics dominated by diffusion or adsorption processes,[39] while smaller τ reflected faster dynamics like charge transfer or electric double-layer (EDL) charging at higher frequencies.[40]

Figure 3e reveals a voltage-dependent evolution of τ distribution: in the high-frequency domain ($\log(\tau) = 0.001–0.1$), peak intensity initially increases under low overpotentials as applied voltage activates proton reduction ($H^+ + e^- \rightarrow$ Hads) and rapid EDL charging. This phase induces abrupt depletion of interfacial ions (H^+/OH^-), generating steep concentration gradients. Although Fickian diffusion driving force is enhanced, unstable laminar flow restricts ionic replenishment—manifested as rising diffusion impedance and mass-transport-limited currents. As voltage further increases, the high-frequency peak diminishes due to Ni^{3+} reduction to Ni^{2+} at catalytic surfaces, which lowers electron transfer resistance. The persistent high-frequency component ($\log(\tau) = 0.001–0.01$) corresponds to omnipresent EDL charging accompanying all electron-transfer processes.[39,41] Meanwhile, near-baseline mid-frequency peaks ($\log(\tau) = 0.01–1$) confirm negligible mass-transport limitations, indicating sufficient bulk ion mobility. Low-frequency peaks ($\log(\tau) = 1–100$) consistently decayed as higher overpotentials shift the reaction pathway from adsorption-limited H^+ electroreduction (initial Volmer step: $H_2O + e^- \rightarrow$ Hads + OH^-) to diffusion-controlled bimolecular recombination (Tafel step: 2Hads → H_2). This transition reduces dependence on adsorbed intermediates, thereby lowering impedance. The systematic shift of $\log(\tau)$ from low to high frequencies maps the interplay of EDL capacitance (Cdl), electrolyte resistance, and dynamic coverage fluctuations of adsorption intermediates.

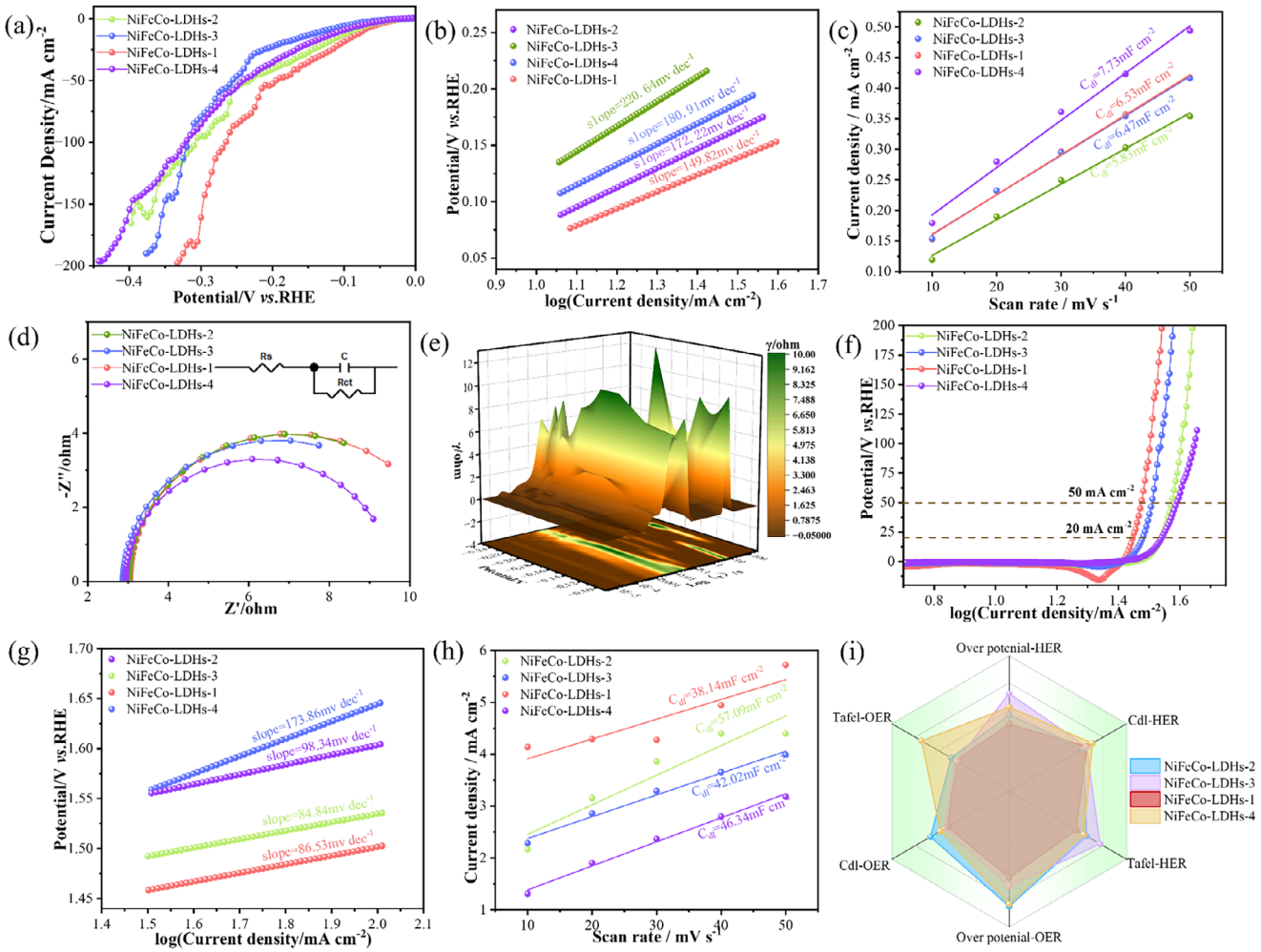

Figure 3. Electrocatalytic performances in 1.0 KOH solutions. HER performances. a) LSV curves for HER. b) Tafel plots. c) CV curves of double-layer capacitance (Cdl). d) Nyquist plots. e) DRT plot. OER performances. f) LSV curves for OER. g) Tafel plots. h) CV curves of double-layer capacitance (Cdl). i) Radar Chart.

In summary, DRT analysis of the NiFeCo-LDHs-1 electrocatalyst reveals critical kinetic enhancements under increasing potentials. The low-frequency regime demonstrates a mechanistic transition to faster diffusion-controlled pathways, shifting dominance from the Volmer step (H^+ adsorption) to the Tafel step (bimolecular recombination). This evolution reduces dependence on adsorbed intermediates, significantly lowering impedance. Concurrently, Ni^{3+} reduction at high frequencies enhances electron transport by reducing charge-transfer resistance. These synergistic effects markedly boost both catalytic efficiency and charge transfer kinetics. Crucially, chrono potentiometric stability testing (Figure S1b) confirms exceptional durability: the catalyst maintains stable HER performance at a constant current density of -10 mA cm^{-2} for 72 h, underscoring the structural robustness of NiFeCo-LDHs-1 nanosheets as a key performance metric for practical applications.

Complementary OER measurements of NiFeCo-LDHs-1 in 1.0 M KOH demonstrate exceptional catalytic activity, exhibiting a substantially lower overpotential of 217.3 mV at 20 mA cm^{-2} compared to NiFeCo-LDHs-2 (310.3 mV), NiFeCo-LDHs-3 (249.3 mV), and NiFeCo-LDHs-4 (311.3 mV) (Figure 3f). Kinetic analysis via Tafel slopes (Figure 3g) reveals that NiFeCo-LDHs-1 (86.53 mV dec^{-1}) significantly outperforms its counterparts, with the minimized slope indicating accelerated charge transfer kinetics attributed to optimized Ni doping. Figure 3h shows the electrochemical active surface area (ECSA) of the as-prepared electrocatalysts. Nyquist plots in Figure 3i highlight distinctive charge-transport characteristics, where NiFeCo-LDHs-1 exhibits a steeper low-frequency slope, suggestive of higher ion diffusion resistance yet mitigated by superior bulk conductivity. Figure 3i shows the comprehensive performance comparison of the as-prepared electrode materials, indicating that the NiFeCo-LDHs-1 generally outperforms other electrode materials.

While NiFeCo-LDHs-1 exhibits exceptional bifunctional HER/OER activity in conventional 1.0 M KOH, large-scale hydrogen production places unsustainable pressure on scarce freshwater resources.[42,43] Given seawater constitutes 96.5% of Earth's water reserves, we evaluated this catalyst in alkaline seawater electrolyte (1.0 M KOH + natural seawater, pH 13.51) to probe its viability for sustainable hydrogen generation.

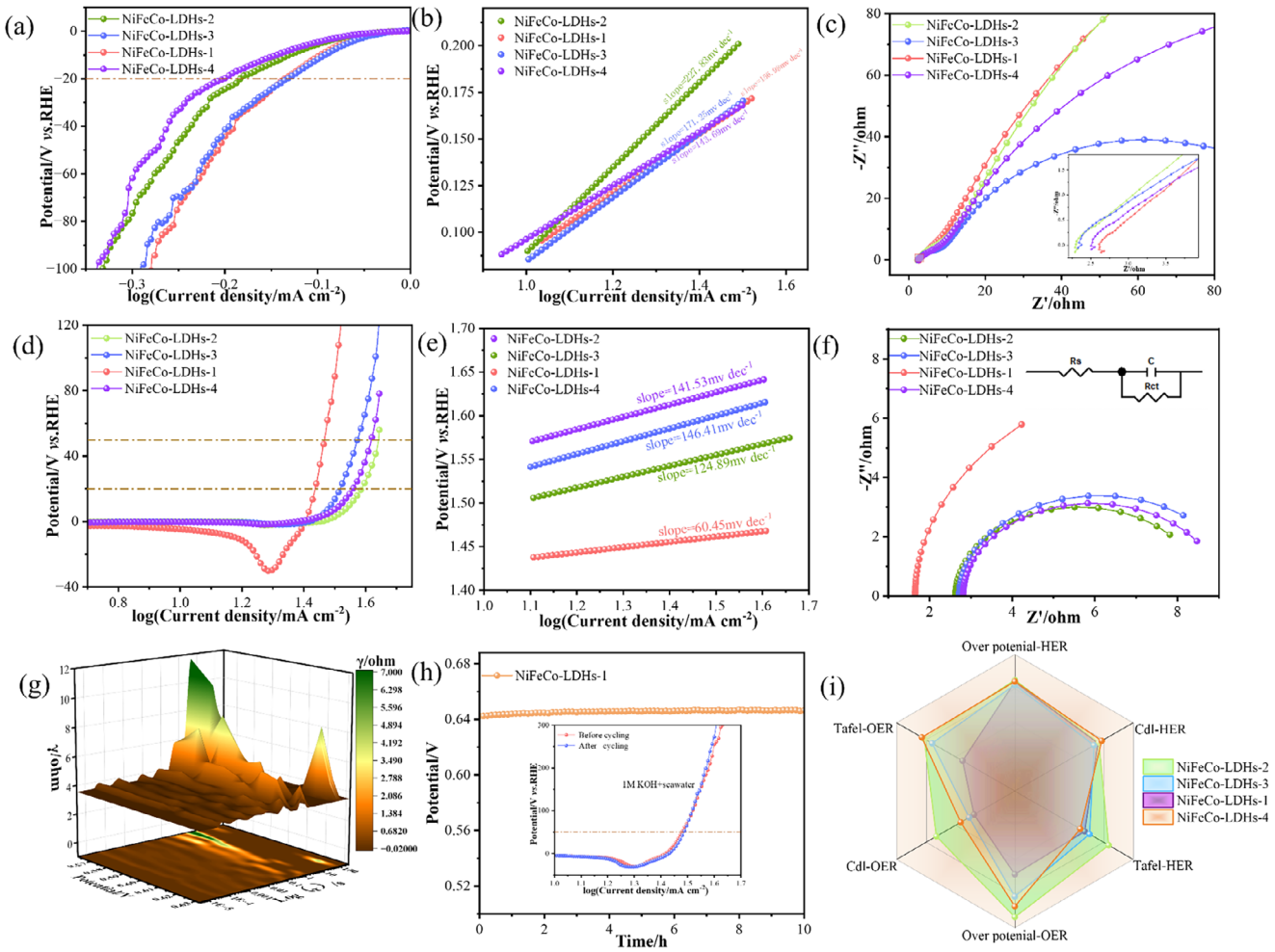

Figure 4. Electrocatalytic performances of the NiFeCo-LDHs-1 electrocatalysts in alkaline seawater. HER performances. a) LSV curves for HER. b) Tafel plots. c) Nyquist plots. OER performances. d) LSV curves for OER. e) Tafel plots. f) Nyquist plots. g) DRT plot. h) Chronoamperometric stability tests of the OER i) Radar Chart.

The transition addresses two critical imperatives: leveraging abundant seawater to alleviate freshwater dependency, and advancing electrocatalyst design for energy-efficient saline water splitting - a crucial pathway toward sustainable clean energy transition.

Electrochemical HER evaluation in alkaline seawater (1.0 M KOH + natural seawater) was conducted using a three-electrode system. As shown in the IR-corrected LSV curves (scan rate: 2 mV s^{-1}, Figure 4a), NiFeCo-LDHs-1 exhibits exceptional activity with an overpotential of 109.5 mV at -10 mA cm^{-2}, outperforming NiFeCo-LDHs-2 (142.5 mV) and NiFeCo-LDHs-4 (155.5 mV). Crucially, while NiFeCo-LDHs-3 shows a marginally lower overpotential (104.5 mV) at this current density, Furthermore, as the current density increases, the overpotential required by NiFeCo-LDHs-1 becomes the lowest among the samples, indicating its suitability for applications under high-current-density operating conditions.NiFeCo-LDHs-1 demonstrates superior kinetics and mass transport - evidenced by its significantly lower Tafel slope (149.82 mV dec^{-1} versus competitors, Figure 4b) and larger ECSA (6.26 mF cm^{-2}, Figure S2a). The advantage amplifies at industrial-relevant current densities: at -50 and -100 mA cm^{-2}, NiFeCo-LDHs-1 achieves remarkably low overpotentials of 219.5 and 291.5 mV respectively. A low Electrochemical Active Surface Area (ECSA) does not necessarily correlate with a poor Tafel slope. In this case, the catalyst possesses high intrinsic activity, which is why the OER Tafel analysis indicates superior reaction kinetics. The complex composition of seawater, which includes various cations (e.g., Mg^{2+} and Ca^{2+}) and inorganic salts, must be considered. During the OER process in this medium, precipitates such as carbonates, hydroxides, or hydroxychlorides (e.g., $Mg(OH)_2$, $CaCO_3$) can form on the surface of a highly active catalyst. These deposits can physically block active sites or pores, leading to a measured ECSA that is smaller than the material's true physical surface area. To demonstrate the material's intrinsic activity, its performance in a simpler alkaline medium is notable. It requires low overpotentials of only 204.3 mV @ 10 mA cm^{-2} and 217.3 mV @ 20 mA cm^{-2}, and it displays a small Tafel slope of 86.53 mV dec^{-1}, confirming its exceptionally fast intrinsic reaction kinetics. Remarkably, despite the risks of side reactions and precipitation in the alkaline seawater medium, the material still exhibited outstanding performance (Figure 4d). It required an overpotential of just 207.5 mV to achieve 20 mA cm^{-2} and

possessed the lowest Tafel slope among the tested samples (Figure 4e). This performance significantly surpasses that of the other compositional ratios of this material and is superior to data from many OER catalysts reported in the literature under similarly complex conditions. It is important to emphasize that this excellent performance was achieved in the presence of and despite the influence of impurities inherent to seawater. Figure 4c shows the electrochemical impedance spectroscopy (EIS) Nyquist plots, reflecting the charge transfer capabilities of the respective electrocatalysts. In the high-frequency region, the NiFeCo-LDHs-1 sample exhibits a smaller semicircular diameter, indicating a lower charge transfer resistance. In the low-frequency region, the NiFeCo-LDHs-1 electrode displayed a steeper slope than electrodes with other NiFeCo-LDHs ratios, demonstrating lower diffusion resistance and intrinsic resistance. These characteristics collectively highlight its superior charge transfer capability and conductivity. Overall, the NiFeCo-LDHs-1 sample exhibits excellent electrocatalytic performance.

The oxygen evolution reaction (OER) performance of the samples was also evaluated in a 1.0 M KOH + natural seawater electrolyte. As depicted in Figure 4d, the NiFeCo-LDHs-1 nanosheets exhibit a substantially lower overpotential of 207.5 mV at 20 mA cm^{-2} compared to NiFeCo-LDHs-2 (356.5 mV), NiFeCo-LDHs-3 (288.5 mV), and NiFeCo-LDHs-4 (329.5 mV), indicating significantly enhanced OER electrocatalytic activity for the Ni:Fe:Co molar ratio of 1:1:1. Moreover, its superiority becomes increasingly pronounced at higher current densities, where the overpotential gap widens markedly. Tafel analysis (Figure 4e) shows the reaction kinetics follow the order (NiFeCo-LDHs-1 > NiFeCo-LDHs-3 > NiFeCo-LDHs-4 > NiFeCo-LDHs-2), confirming NiFeCo-LDHs-1 possesses the fastest kinetics. The electrochemical active surface area (ECSA) of NiFeCo-LDHs-1, determined from capacitance measurements (Figure S2b), is 0.01898 mF cm^{-2}. The equivalent circuit fitting (Figure 4f) shows that NiFeCo-LDHs-1 has a small high-frequency intercept with the real axis, indicating a low solution contact resistance (Rs) of only 1.65 Ω. However, its Rct value is relatively high at 15.6 Ω. This might be because the active sites that should be exposed on the NiFeCo-LDHs are partially or completely covered by agglomerates. Charge must first "penetrate" or "bypass" these agglomerated low-activity regions to react, which significantly increases the difficulty and resistance of charge transfer. Furthermore, these agglomerates disrupt the originally uniform and efficient electrode interface structure, creating non-uniform or inefficient charge transport channels. The agglomeration leads to a more complex catalyst surface and potential pore blockage, which restricts the pathways for electrolyte ions to reach active sites and for products to depart, thereby indirectly worsening the environment required for efficient charge transfer.

Figure S2c presents the Bode phase angle plot of the NiFeCo-LDHs-1 sample for the oxygen evolution reaction (OER). At low potentials (<1.50 V versus RHE), no significant decline in phase angle was observed in the low-frequency region, indicating that the OER has not commenced substantially. When the applied potential exceeds 1.55 V versus RHE, a rapid decrease in the phase angle occurs within the low-frequency range, signifying the onset of the OER process. As the potential is further increased, the magnitude of the phase angle decrease becomes progressively more pronounced, demonstrating an acceleration in the OER reaction kinetics. The decline in phase angle within the low-frequency region reflects the dominance of the charge transfer process at the electrode interface.[41] The significant reduction observed at higher potentials indicates lower charge transfer resistance and substantially enhanced catalytic activity. The doping of Ni modifies the electronic structure of the NiFeCo-LDHs-1, optimizing the adsorption energies of oxygen intermediates. This modification effectively lowers the OER onset potential and accelerates the reaction kinetics.

Relaxation Time Distribution (DRT) analysis (Figure 4g, with voltage on *X*-axis, log(τ) representing frequency region on *Y*-axis, and γ ($\Omega \cdot s^{-1}$) quantifying the contribution of each polarization process to the total impedance on *Z*-axis[40,44,45]) provided deeper insight into kinetic processes. The low-frequency region (log(τ) between 1 and 100) exhibits a single intensive peak specifically at high voltages. This phenomenon arises due to the low diffusion coefficient of OH^- ions in alkaline media, which readily leads to concentration polarization under high current densities. Consequently, mass transport limitations dominate the low-frequency impedance response. Furthermore, doped Ni^{2+} was oxidized to higher valence Ni^{3+} states at high anodic potentials in the alkaline environment. This introduces additional resistance associated with lattice oxygen migration. The combined effect shifts the reaction dynamics towards a single dominant relaxation process in the low-frequency region, resulting in a prominent single peak and increased impedance in the Nyquist plot.[46] During the shift towards the mid-frequency region (corresponding to log(τ) ≈ 0.1), a distinct peak emerges at lower potentials. As the applied potential increases, the intensity of this peak progressively diminishes. The peak in the mid-frequency region primarily corresponds to the key step of intermediate conversion, such as the deprotonation step (*OH→*O). At lower potentials, the insufficient overpotential results in a substantial energy barrier that must be overcome for this intermediate conversion to proceed. Consequently, the charge transfer resistance associated with this step is significantly high. Furthermore, the slower reaction rates at these potentials amplify the resistive contribution from this process. This combination manifests as the prominent peak observed in the mid-frequency region at low potentials. With increasing applied potential, overcoming the energy barrier becomes more facile, accelerating the intermediate conversion kinetics. As a direct result of this faster kinetics, the intensity of the corresponding DRT peak decreases. Notably, a new peak emerges at the interface between mid and high frequencies during voltage scanning. This signal corresponds to voltage-driven surface reconstruction forming higher-valent oxide species (e.g., CoOOH, NiOOH), which enhances interfacial ion migration.[47,48] These reconstructed oxide layers create additional pathways for charge transport and storage, significantly boosting charge transfer kinetics; specifically, the formed CoOOH/NiOOH features a high intrinsic electrochemical activity, improving interfacial proton-coupled electron transfer (PCET) efficiency that accelerates overall catalysis. As the peak shifts toward the high-frequency region, a noticeable decrease in peak intensity becomes apparent, indicating that the activation

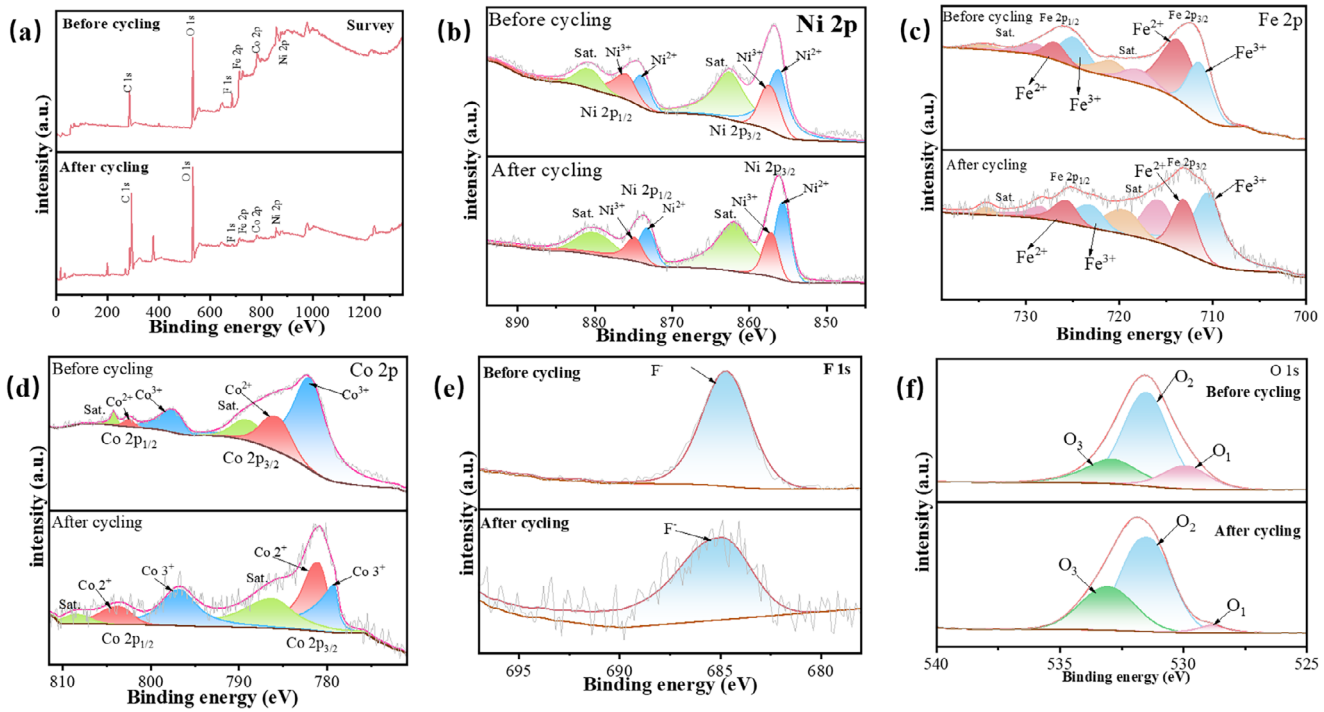

Figure 5. Structure characterization of the NiFeCo-LDHs-1catalysts after cycle for OER. a) XPS survey spectrum. b) XPS of Ni 2p. c) Fe 2p. d) Co 2p. e) F 1 s. f) O 1 s.

energy barrier for this step has been effectively overcome, and the reaction rate has significantly increased. No distinct peaks and only minor fluctuations are observed across the entire high-frequency region. This suggests that the kinetic resistance associated with processes in the high-frequency region—such as electron transport or electrical double-layer processes—is extremely low and highly stable. Furthermore, the processes corresponding to this region are not the rate-determining steps, and their impedance contributions remain voltage-insensitive. In summary, the DRT analysis of the OER process on NiFeCo-LDHs-1 provides direct evidence for the superior electron transport performance of this catalyst. Chromo potentiometric stability testing over 10 h (Figure 4h) demonstrates satisfactory operational robustness for NiFeCo-LDHs-1, with the overpotential at a fixed current density showing no significant degradation in the inset LSV comparison. Evaluation through the radar chart (Figure 4i) clearly illustrates the superior bifunctional electrocatalytic performance of NiFeCo-LDHs-1 towards both the hydrogen evolution reaction HER and OER in alkaline seawater. Overall, the NiFeCo-LDHs-1 sample exhibits outstanding electrocatalytic characteristics.

The elemental composition and chemical states of the synthesized NiFeCo-LDH-1 product before and after cyclic stability testing were investigated using X-ray photoelectron spectroscopy (XPS). The survey spectra (Figure 5a) confirmed the presence of Co, Fe, Ni, F, and O in both states. Post-cycling analysis revealed distinct changes in the metal oxidation states. Figure 5b reveals that the Ni 2p peaks shifted towards lower binding energies after cycling. The peaks located at 874.89 and 857.12 eV decreased by 0.99 and 0.22 eV, respectively, compared to their positions before cycling, indicating the reduction of Ni ions from Ni^{3+} to Ni^{2+} after cycling. The Ni^{2+} peaks corresponding to both Ni $2p_{1/2}$ and Ni $2p_{3/2}$ core levels shifted overall towards lower binding energies by 0.72 and 0.47 eV, respectively. Figure 5c indicates that the Fe 2p spectra of the two samples present largely consistent profiles. After cycling, the characteristic peaks for Fe^{3+} are observed at 734.22 and 719.31 eV, exhibiting decreases of 0.21 and 1.43 eV compared to the pre-cycling peaks, respectively. Peaks at 728.42 and 715.63 eV represent Fe^{2+} also showed an overall decrease in binding energy. This shift of Fe 2p peaks towards lower binding energies after cycling demonstrates the reduction of Fe ions from Fe^{3+} to Fe^{2+}.Figure 5d shows that after cycling, the binding energies for Co^{3+} and Co^{2+} in the Co $2p_{3/2}$ region are located at 779.23 and 781.02 eV, respectively, representing decreases of 2.61 and 4.61 eV compared to values before cycling. The binding energy for Co^{3+} in the Co $2p_{1/2}$ region decreased by 1.23 eV, confirming the continued presence of both Co^{2+} and Co^{3+}.[31,32] Notably, the Co 2p spectrum shifted towards higher binding energies overall, suggesting an increased proportion of Co^{3+} after cycling. The F 1 s peak (Figure 5e) was consistently observed at 684.97 eV after cycling, confirming the presence of F^- ions within the compound. The lack of binding energy shift indicates the F^- species remained structurally stable during electrocatalysis, likely playing an environmental modulation role. Analysis of the O 1 s spectrum (Figure 5f) identified three distinct components: lattice oxygen (O_1, 528.84 eV), oxygen vacancies (O_2, 531.45 eV), and hydroxyl groups/hydroxide species (O_3, 533.08 eV). Crucially, the significant increase in the intensity of the hydroxyl-related peak (O_3) post-cycling demonstrates the progressive conversion of

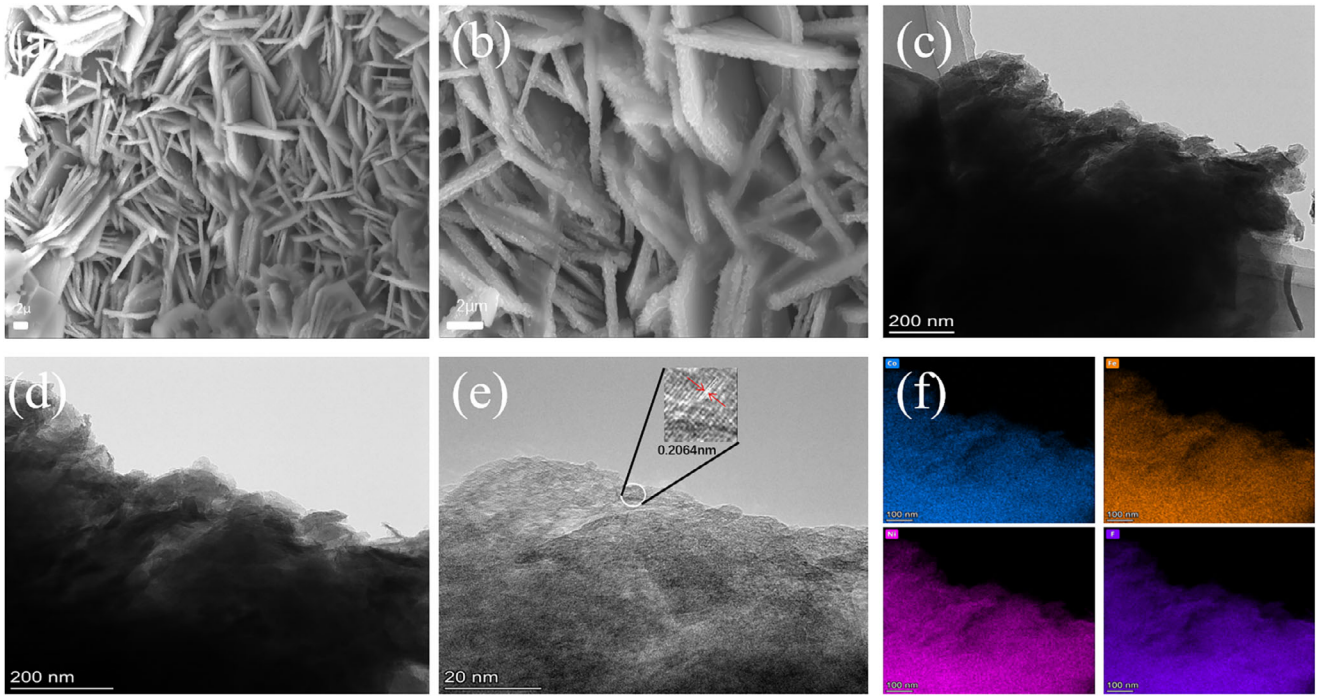

Figure 6. Structure characterization of the NiFeCo-LDHs-1 catalysts after cycle for OER. a,b) SEM images, c–-e) TEM images, f) elemental mapping images.

Table 1. Table comparing overall water splitting performance: Simulated seawater versus control conditions.

Performance Parameters	1.0 M KOH	1.0 M KOH + seawater	Performance Trend
HER lsv (η@-10mAcm^{-2})	74.3mV	109.5mV	↑47.4%
OER lsv (η@ 20 mA cm^{-2})	217.3mV	207.5mV	↓4.5%
Total Water-Splitting Voltage (V@100 mA cm^{-2})	1.964V	2.046V	↑ 4.2%
HER Tafel	149.82 mV dec^{-1}	156.98 mV dec^{-1}	↑ 4.8%
OER Tafel	86.53 mV dec^{-1}	60.45 mV dec^{-1}	↓43.1%
HER Cdl	6.53mF cm^{-2}	6.26mF cm^{-2}	↓4.3%
OER Cdl	38.14mF cm^{-2}	18.98mF cm^{-2}	↓100.9%

the active phase into hydroxide/oxyhydroxide species during electrocatalysis. The formation of M-OOH intermediates (where M = Ni, Fe, Co) enhances OER efficiency by providing increased active sites.

Scanning electron microscopy (SEM) images of the NiFeCo-LDHs-1 electrode after OER cycling tests (Figure 6a,b) confirm that the nanosheet architecture remains largely intact, with the overall morphology showing minimal alteration compared to its pre-cycling state. This structural retention provides direct morphological evidence of its favorable cycling stability. Further examination by transmission electron microscopy (TEM) and high-resolution TEM (HRTEM) corroborates these findings. Figure 6c,d present transmission electron microscopy (TEM) images and corresponding local enlargements. Further observations reveal surface roughness of the nanosheets with increased overall thickness, while the fundamental morphology remains intact after cycling. The corresponding HRTEM image (Figure 6e) displays clear lattice fringes with a measured interplanar spacing of 0.2064 nm. Elemental mapping analysis (Figure 6f) demonstrates the continued homogeneous spatial distribution of nickel, cobalt, and iron throughout the nanosheets after cycling, further indicating the robust structural integrity and compositional stability of the synthesized material. Collectively, these electron microscopy results substantiate the excellent morphological and structural durability of the NiFeCo-LDHs-1 catalyst during prolonged OER operation.

This material exhibited outstanding electrocatalytic activity for both the hydrogen evolution reaction (HER) and oxygen evolution reaction (OER) in alkaline solutions as well as simulated alkaline seawater environments. This robust dual-functionality underscores its significant potential as an efficient and stable bifunctional electrocatalyst for overall water splitting applications. The development of such versatile catalytic systems holds considerable value for clean energy technology innovation,

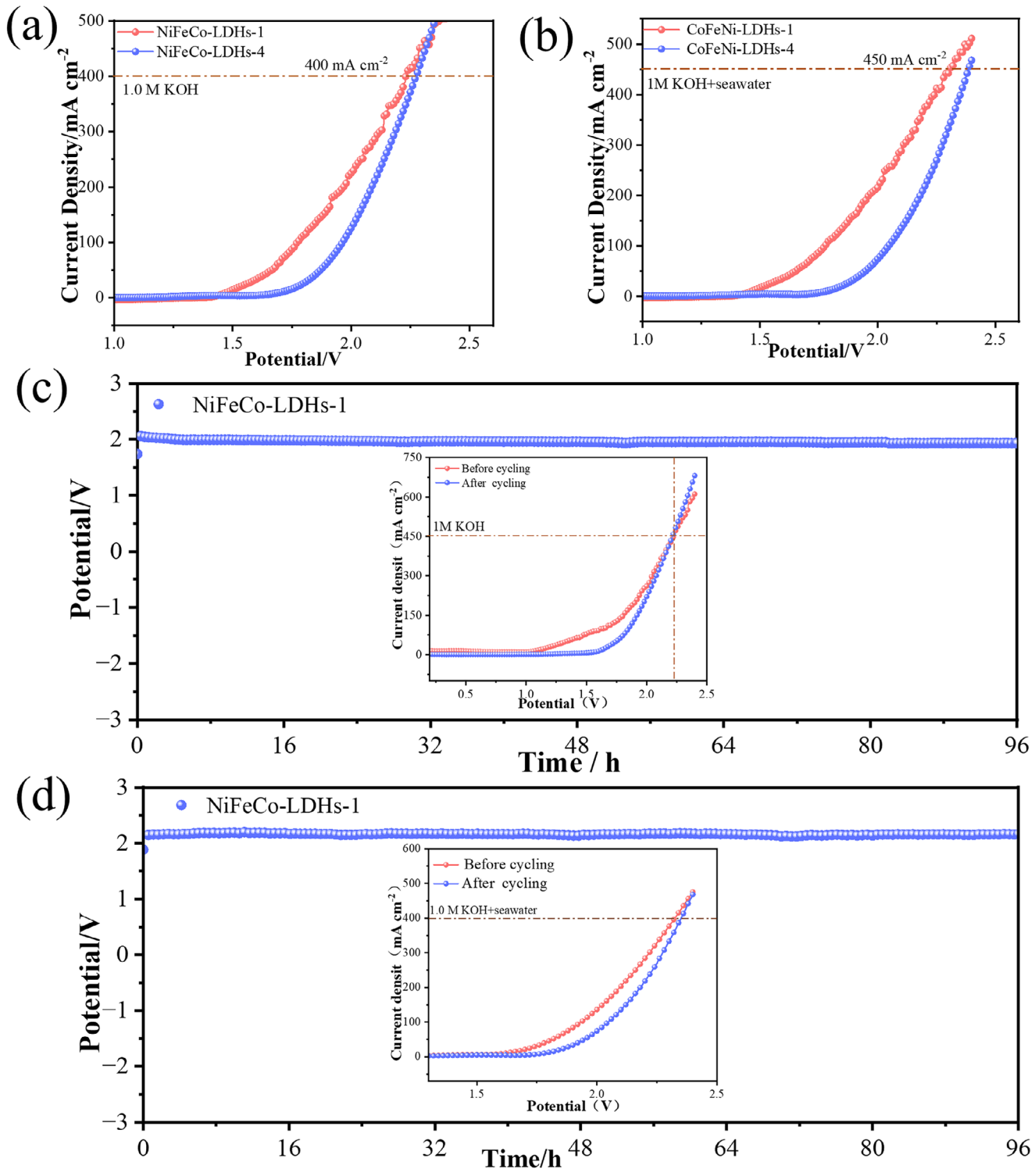

Figure 7. Overall water splitting performance of the electrocatalysts. a) LSV curves in 1.0 M KOH. b) LSV curves in seawater. c) chronoamperometric stability tests of the 1.0 M KOH, d) chronoamperometric stability tests of the seawater.

offering a viable technological avenue for large-scale hydrogen production by simultaneously accelerating the kinetics of water dissociation. Notably, the catalyst maintains exceptional performance under simulated seawater conditions. This capability not only broadens the scope for high-value utilization of marine resources but also accentuates its unique advantages within coastal and offshore renewable energy systems. By effectively leveraging abundant seawater resources, this catalyst provides an innovative solution for clean energy supply within marine economic zones (Table 1).

To evaluate the practical applicability of the electrocatalyst in water splitting, the as-prepared samples were assembled as both anode and cathode in a customized electrolyzer. Linear sweep voltammetry (LSV) curves recorded in 1.0 M KOH electrolyte (Figure 7a) demonstrate that the NiFeCo-LDHs-1 catalyst achieved cell voltages of 2.163 V at current densities of 400 mA cm^{-2}, respectively. Under simulated alkaline seawater conditions (Figure 7b), it required only 2.249 V to reach identical current densities. Both sets of metrics surpass the performance of NiFeCo-LDHs-4 (2.274 V in KOH and 2.351 V in seawater at 400 mA cm^{-2}), confirming NiFeCo-LDHs-1′s superior overall water splitting efficiency. Notably, the NiFeCo-LDHs-1 electrode exhibited exceptional electrochemical durability in 1.0 M KOH (Figure 7c). After 96 h of continuous operation, it maintains stable water-splitting activity with the overall water-splitting potential declining from an initial 2.163 to 2.241 V post-stability testing. More significantly, in simulated seawater electrolyte (Figure 7d), the material displays remarkable resistance to performance degradation during equivalent durability testing. The polarization curve reveals no increase in overpotential compared to the baseline, indicating minimal impact on catalytic activity after prolonged operation. This phenomenon not only verifies the catalyst's structural robustness in chloride-containing environments but also underscores its engineering potential for sustained high-efficiency energy conversion in seawater electrolysis applications.

3. Conclusion

In this study, a layered NiFeCo-LDH-1 bifunctional electrocatalyst was successfully synthesized via a one-step hydrothermal approach. Experimental characterization confirms that the optimized NiFeCo-LDHs-1 composite system possesses a high density of electroactive sites and a tailored electronic structure. Electrochemical tests demonstrate its superior dual-functional catalytic performance in both alkaline (1.0 M KOH) and simulated seawater electrolytes: in KOH, it exhibited low overpotentials of merely 74 mV for HER at -10 mA cm^{-2} and 217.3 mV for OER at 20 mA cm^{-2}, while in alkaline seawater, it achieves 109.5 mV (HER at -10 mA cm^{-2}) and 207.5 mV (OER at 20 mA cm^{-2}), demonstrating exceptional catalytic activity. Moreover, it requires only 2.163 V cell voltage for overall water splitting at 400 mA cm^{-2}, with negligible performance degradation ($\Delta V < 0.15$ V) during 96-h continuous operation. This outstanding stability stems from the high electroactive. Our work provides new insights into and establishes a promising materials design paradigm for developing highly efficient bifunctional water-splitting catalysts suitable for complex ionic environments.

Supporting Information

Supporting Information is available from the author.

Acknowledgments

This work was supported by the Project of Education Department of Liaoning Province (No. LJKMZ20220959), the National Natural Science Foundation of China (No. 51971106). Science and Technology Innovation Talent Project of Liaoning Provincial Department of Education (LJ222411632049 and LJ222411632081).

Conflict of Interests

The authors declare no conflict of interest.

Data Availability Statement

The data that support the findings of this study are available on request from the corresponding author. The data are not publicly available due to privacy or ethical restrictions.

Keywords: Alkaline seawater electrolysis · Electrocat-alytic performance · NiFeCo-LDHs composite material · Overpotential

[1] P. Poizot, F. Dolhem, *Energy Environ. Sci.* **2011**, *4*, 2003–2019, https://doi.org/10.1039/c0ee00731e.
[2] R. J. Detz, J. N. H. Reek, B. C. C. van der Zwaan, *Energy Environ. Sci.* **2018**, *11*, 1653–1669, https://doi.org/10.1039/C8EE00111A.
[3] Z. Yang, W. Zhao, J. Wang, R. Chen, X. Li, T. Xue, K. Zhang, J. Zhao, *Sci. Adv. Mater.* **2018**, *10*, 215–219, https://doi.org/10.1166/sam.2018.2954.
[4] J. Chi, H. Yu, *Chin. J. Catal.* **2018**, *39*, 390–394, https://doi.org/10.1016/S1872-2067(17)62949-8.
[5] S. Anwar, F. Khan, Y. Zhang, A. Djire, *Int. J. Hydrogen Energy* **2021**, *46*, 32284–32317, https://doi.org/10.1016/j.ijhydene.2021.06.191.
[6] M. Pein, N. C. Neumann, L. J. Venstrom, J. Vieten, M. Roeb, C. Sattler, *Int. J. Hydrogen Energy* **2021**, *46*, 24909–24918, https://doi.org/10.1016/j.ijhydene.2021.05.036.
[7] S. Shiva Kumar, V. Himabindu, *Mater. Sci. Energy Technol.* **2019**, *2*, 442–454.
[8] E. L. Hu, Y. F. Feng, J. W. Nai, D. Zhao, Y. Hu, X. W. Lou, *Energy Environ. Sci.* **2018**, *11*, 872–880, https://doi.org/10.1039/C8EE00076J.
[9] M. I. Abdullah, A. Hameed, N. Zhang, M. M. Ma, *Adv. Mater. Interfaces* **2019**, *6*, 1900586, https://doi.org/10.1002/admi.201900586.
[10] G. Li, J. Yu, J. Jia, L. Yang, L. Zhao, W. J. Zhou, H. Liu, *Adv. Funct. Mater.* **2018**, *28*, 1801332, https://doi.org/10.1002/adfm.201801332.
[11] S. Qin, J. Sun, X. Meng, *Nano Energy* **2019**, *62*, 338–347.
[12] J. Tian, Q. Liu, A. M. Asiri, X. Sun, *J. Am. Chem. Soc.* **2014**, *136*, 7587–7590, https://doi.org/10.1021/ja503372r.
[13] N. T. Suen, S. F. Hung, Q. Quan, N. Zhang, Y. J. Xu, H. M. Chen, *Chem. Soc. Rev.* **2017**, *46*, 337–365, https://doi.org/10.1039/C6CS00328A.
[14] R. Nandan, A. Gautam, S. Tripathi, K. K. Nanda, *J. Mater. Chem. A* **2018**, *6*, 8537–8548, https://doi.org/10.1039/C8TA01938J.
[15] K. Wang, X. Wang, Z. Li, B. Yang, M. Ling, X. Gao, J. Lu, Q. Shi, L. Lei, G. Wu, Y. Hou, *Nano Energy* **2020**, *77*, 105162, https://doi.org/10.1016/j.nanoen.2020.105162.
[16] F. Guo, Z. Liu, J. Xiao, X. Zeng, C. Zhang, Y. Lin, P. Dong, T. Liu, Y. Zhang, M. Li, *Chem. Eng. J.* **2022**, *446*, 137111, https://doi.org/10.1016/j.cej.2022.137111.
[17] Y. Dong, C. W. Oloman, E. L. Gyenge, J. Su, L. Chen, *Nanoscale* **2020**, *12*, 9924–9934, https://doi.org/10.1039/D0NR02187C.
[18] C. Zhang, Z. Xu, Y. Yu, A. Long, X. Ge, Y. Song, Y. An, Y. Gu, *Electrochim. Acta* **2022**, *424*, 140613, https://doi.org/10.1016/j.electacta.2022.140613.
[19] J. Zhang, W.-J. Jiang, S. Niu, H. Zhang, J. Liu, H. Li, G.-F. Huang, L. Jiang, W.-Q. Huang, J.-S. Hu, W. Hu, *Adv. Mater.* **2020**, *32*, 1906015–1906030, https://doi.org/10.1002/adma.201906015.

[20] M. S. Burke, L. J. Enman, A. S. Batchellor, S. Zou, S. W. Boettcher, *Chem. Mater.* **2015**, *27*, 7549–7558, https://doi.org/10.1021/acs.chemmater.5b03148.
[21] M. Cai, Q. Liu, Z. Xue, Y. Li, Y. Fan, A. Huang, M. R. Li, M. Croft, T. A. Tyson, Z. Ke, *J. Mater. Chem. A* **2020**, *8*, 190–195, https://doi.org/10.1039/C9TA09397D.
[22] H. Wang, J. Li, K. Li, Y. Lin, J. Chen, L. Gao, V. Nicolosi, X. Xiao, J. M. Lee, *Chem. Soc. Rev.* **2021**, *50*, 1354–1390, https://doi.org/10.1039/D0CS00415D.
[23] D. Tian, S. R. Denny, K. Li, H. Wang, S. Kattel, J. G. Chen, *Chem. Soc. Rev.* **2021**, *50*, 12338–12376, https://doi.org/10.1039/D1CS00590A.
[24] R. Li, P. Ren, P. Yang, Y. Li, H. Zhang, A. Liu, S. Wen, J. Zhang, M. An, *J. Colloid Interface Sci.* **2022**, *631*, 173–181, https://doi.org/10.1016/j.jcis.2022.11.033.
[25] P. Liu, Y. Pu, *Int. J. Hydrogen Energy* **2021**, *46*, 197–207.
[26] K. Lemoine, J. Lhoste, A. Hémon-Ribaud, N. Heidary, V. Maisonneuve, A. Guiet, N. Kornienko, *Chem. Sci.* **2019**, *10*, 9209–9218, https://doi.org/10.1039/C9SC04027G.
[27] Z. Lu, Z. Zhou, S. Li, G. Huang, T. He, J. Cai, M. Jin, Y. Li, X. Zhang, S. Li, *Coatings* **2023**, *13*, 726, https://doi.org/10.3390/coatings13040726.
[28] J. Zhang, S. Zhang, Z. Zhang, J. Wang, Z. Zhang, G. Cheng, *J. Alloys Compd.* **2023**, *939*, 168753, https://doi.org/10.1016/j.jallcom.2023.168753.
[29] J. Y. Chen, C. Fan, X. Y. Hu, *Small* **2019**, *15*, 1901518–1901538, https://doi.org/10.1002/smll.201901518.
[30] J. Wang, R. Xu, Y. L. Sun, *J. Energy Chem.* **2021**, *55*, 162–168, https://doi.org/10.1016/j.jechem.2020.07.010.
[31] D. P. Zhao, M. Z. Dai, Y. Zhao, *Nano Energy* **2020**, *72*, 104715, https://doi.org/10.1016/j.nanoen.2020.104715.
[32] W. Xi, G. Yan, H. Tan, *Dalton Trans.* **2018**, *47*, 8787–8793, https://doi.org/10.1039/C8DT00765A.
[33] K. Obata, K. Takanabe, *Angew. Chem.* **2018**, *130*, 1632–1636, https://doi.org/10.1002/ange.201712121.
[34] B. B. Gicha, L. T. Tufa, M. Goddati, Y. Lee, B. F. Banti, N. N. Njoku, S. You, J. Lee, A. C. S. Appl, *Nano Mater* **2024**, *7*, 13308–13318.
[35] Y. Wang, Y. Zhang, Y. Li, X. Yang, T. Liu, M. Zhang, X. Zhang, A. C. S. Appl, *Nano Mater* **2022**, *5*, 7887–7895.
[36] Z. Lu, Z. Zhou, S. Li, G. Huang, T. He, J. Cai, M. Jin, Y. Li, X. Zhang, S. Li, C. Chen, G. Wang, *Catalysts* **2022**, *12*, 1241.
[37] L. Guo, J. Chi, T. Cui, J. Zhu, Y. Xia, H. Guo, J. Lai, L. Wang, *Adv. Energy Mater.* **2024**, *14*, 2304107.
[38] S. Wan, M. Saccoccio, C. Chen, F. Ciucci, *Electrochim. Acta* **2015**, *184*, 483–499, https://doi.org/10.1016/j.electacta.2015.09.097.
[39] W. J. Wang, W. T. Huang, Y. Q. Li, R. Z. Wang, L. Zhuang, Q. F. Zhang, *J. Electrochem* **2020**, *26*, 16–36.
[40] J. Chen, E. Quattrocchi, F. Ciucci, *Chem* **2023**, *9*, 2267–2281, https://doi.org/10.1016/j.chempr.2023.04.022.
[41] C. Chang, R. Ren, M. Mu, Z. Zuo, Z. Zou, Z. Zhou, W. Wen, T. Tao, Z. Zhou, L. Lai, K. Kobayashi, Z. Zhang, *Adv. Mater.* **2025**, *37*, 2415393.
[42] O. Guselnikova, A. Trelin, E. Miliutina, R. Elashnikov, P. Saidl, P. Postnikov, Z. Kolska, V. Svorcik, O. Lyutakov, *ACS Appl. Mater. Interfaces* **2020**, *12*, 28110–28119, https://doi.org/10.1021/acsami.0c04029.
[43] L. Li, Z. Zhou, L. Li, Z. Zhuang, J. Bi, J. Chen, Y. Yu, J. Yu, *ACS Sustainable Chem. Eng.* **2019**, *7*, 18574–18581, https://doi.org/10.1021/acssuschemeng.9b04749.
[44] J. Zuo, N. Y. Steiner, Z. Li, D. Hissel, *Appl. Energy* **2025**, *386*, 125543, https://doi.org/10.1016/j.apenergy.2025.125543.
[45] C. Plank, T. Rüther, L. Jahn, *J. Power Sources* **2024**, *594*, 233845, https://doi.org/10.1016/j.jpowsour.2023.233845.
[46] X. Y. Wang, Z. Y. Pan, X. F. Chu, *Angew. Chem., Int. Ed.* **2019**, *58*, 11720–11725, https://doi.org/10.1002/anie.201905543.
[47] M. Fang, D. Han, W. B. Xu, X. X. Zhang, Z. Y. Wang, T. Y. Zhang, Z. Q. Zhang, X. S. Zhao, *Nano Energy* **2019**, *60*, 631–638.
[48] K. Baral, V. Sankar, M. Matatyaho, K. Kushnir, Y. Tsur, *Chem. Sus. Chem.* **2020**, *13*, 5671–5682, https://doi.org/10.1002/cssc.202001503.

Manuscript received: July 14, 2025
Revised manuscript received: September 20, 2025
Version of record online: ■■, ■■